

Electrocatalysis under Conditions of High Mass Transport Rate: Oxygen Reduction on Single Submicrometer-Sized Pt Particles Supported on Carbon

Shengli Chen and Anthony Kucernak*

Department of Chemistry, Imperial College London, London SW7 2AZ, U.K.

Received: September 22, 2003; In Final Form: January 12, 2004

The effect of the mass transport coefficient of reactant and product species during the oxygen reduction reaction, orr, on platinum in an acidic electrolyte has been experimentally examined and kinetically modeled. By using carbon electrodes having electroactive radii on the nanometer scale it is possible to produce single Pt particles having effective radii ranging from several micrometers to several tens of nanometers. As the mass transport coefficient is directly related to the size of these platinum particles, it is possible to examine the effect of mass transport on the orr in regions inaccessible to other experimental techniques. At the smallest of these Pt particles, mass transport coefficients equivalent to a rotating disk electrode at rotation rates (ω) of greater than 10^8 rpm are obtainable. Under low mass transport conditions equivalent to those obtainable using the normal rotating disk technique (i.e., $\omega < 10\,000$ rpm), oxygen reduction is seen to proceed via a four-electron reduction to water as has been reported in the general literature. Under high mass transport conditions about 75% of reactant oxygen molecules are reduced to water with the balance being only reduced as far as hydrogen peroxide. The production of peroxide which this result implies may be an important aspect within the cathode catalyst layer of solid polymer electrolyte fuel cells, as these layers are inherently designed to provide high mass transport coefficients. The oxygen reduction reaction on single catalyst particles is modeled according to the parallel reaction mechanism originally introduced by Wroblowa et al. [Wroblowa, H. S.; Pan, Y. C.; Razumney, J. J. *Electroanal. Chem.* **1976**, *69*, 195]. A general expression is derived to predict the effects of the mass transport rate, surface blockage, and potential on the effective electron-transfer number, n_{eff} , which reflects the average number of electrons produced during the reduction of each dioxygen molecule. It is shown that a pure series (or indirect) reaction mechanism for the four-electron reduction of oxygen on Pt electrodes in sulfuric acid solution is consistent with the experimental results. The kinetics of the orr is analyzed using both Tafel plots and the half-wave potential method. The kinetic parameters extracted from the half-wave potential method are in very good agreement with those extrapolated from the Tafel curves with a -120 mV per decade slope. The complexities involved in the orr kinetics are discussed according to the results obtained on these small single-particle electrodes. Specifically, the effect of the double-layer structure and the role of anion adsorption are considered. It is argued that the electrocatalytic reduction of oxygen involves inner-sphere electron-transfer steps and that its kinetics are affected by the potential profile within the compact double layer, especially inside the inner Helmholtz plane (IHP). Anion adsorption may perturb the orr in a way much more complex than simply blocking the surface sites and may significantly change the potential near the IHP, thereby changing the effective driving potential that the reactant and reaction intermediates experience. This may be partly responsible for the variable apparent values of the transfer coefficient of the orr in different potential regions. A new mechanism for the size effects of catalyst nanoparticles on their electrocatalytic properties toward oxygen reduction is proposed in terms of the particle size tunable structure of the double layer.

1. Introduction

The oxygen reduction reaction, orr, has been the focus of electrochemical studies over many years especially because of its critical role in fuel cells and its complex reaction mechanism.^{1–3} The efficiency of fuel cells is limited on the cathode side by the orr in terms of both the mechanism and its kinetics. In mechanism, the formation of the two-electron reduction product, H_2O_2 , will reduce the effective electron-transfer number (n_{eff}) of the orr. This product may also significantly increase the degradation rate of any organic materials present, for example, the proton conducting solid polymer electrolyte present within a solid polymer electrolyte fuel cell. Poor kinetics of

oxygen reduction leads to a more than 300 mV voltage loss in polymer electrolyte fuel cell under typical operation conditions.³

The rotating ring-disk electrode (RRDE) technique has often been used in studies of the orr because it provides the possibility of probing the formation of H_2O_2 accompanying oxygen reduction and therefore of determining the effective electron-transfer number, n_{eff} . In addition, the rotating electrode technique allows kinetic analysis under steady-state mass transport conditions. The RRDE results have been obtained either on bulk electrodes made of polycrystalline materials,^{4–6} single-crystal electrodes,^{7–12} or from electrodes decorated with small particles.^{13–16} The results obtained from these studies of oxygen reduction on platinum and platinum-based alloy electrodes have been used to support a parallel reaction mechanism with predominantly direct four-electron reduction to water. The forma-

* Corresponding author. E-mail: a.kucernak@imperial.ac.uk. Phone: +44(0)20 75945831. Fax: +44(0)20 75945804.

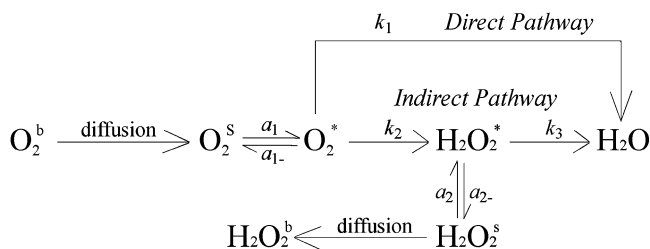


Figure 1. Wroblowa scheme for the pathways of the oxygen reduction reaction.

tion of H_2O_2 during the orr at Pt-based electrodes in acid medium is presumed to occur through an alternative, parallel mechanism and is negligible at potentials outside the hydrogen adsorption region. The reaction scheme proposed by Wroblowa et al.^{1,2,17} has been generally accepted as the mechanism of this parallel reaction (Figure 1). The k 's and a 's in Figure 1 are the overall rate constants for the corresponding reaction or adsorption steps, each of which may contain several elementary steps. The superscripts b, s, and * refer, respectively, to species which are in bulk solution, in the vicinity of the electrode surface, and which are adsorbed on the electrode surface. Also, it has been generally accepted that the rate-determining step in the orr is the first electron-transfer step and that the real reaction rate is an overall result of the coupling of this step with the diffusion and adsorption of oxygen molecules.^{1,2,18–20}

Pt particles of nanometer size supported on carbon are the most widely used catalyst in polymer electrolyte fuel cells. There has been great interest in the relationship between the activity of such catalysts toward the orr and the size of the supported Pt particles.^{21–29} Although great efforts were made, the conclusions varied among the different researchers. The inconsistent results and conclusions are most probably caused by the structural complexity of the electrodes employed. The electrodes used in these studies were prepared by deposition of Pt colloidal particles onto porous graphitic carbon. The catalyst particles produced in this way usually have a layer of stabilizing organic ligand on surface. In addition, other additives, for example, binding materials, have to be used in the production of the electrode.²³ Thus, the results may be modified by such complexities as porous diffusion, particle size distribution, and the presence of additives. A study by Watanaba et al.²³ suggested that the distance between adjacent Pt particles plays a key role in the catalytic activity of the supported Pt nanoparticles electrodes toward the orr. According to this suggestion, the activity of a given mass of Pt particles is controlled by both particle size and particle separation. At constant loading of platinum on carbon, the average particle separation distance decreases with particle size, and thus, even though absolute surface area of the platinum increases, each particle has a greater probability of influencing the diffusion field of adjacent particles. However, the high mass transport rate around individual nanoparticles may lead to formation of H_2O_2 , resulting in loss of activity. It is clear from the reaction scheme shown in Figure 1 that the two-electron reduction to H_2O_2 would become more pronounced when the transport rate of H_2O_2 away from the vicinity of the electrode surface is increased, as this provides a continuous driving force to move the equilibrium toward production of hydrogen peroxide. Although the rotating electrode technique can increase the mass transport rate, the rotation rates used in RRDE studies of the orr (all below 10 000 rpm, limited by cavitation of the electrolyte) might be too low to produce high enough mass transport rates to affect the reaction pathways of the orr.

However, extremely high mass transport rates can be attained at electrodes of reduced size. For example, the mass transport rate would be about 0.2 cm s^{-1} at an electrode of $1 \mu\text{m}$ radius. To attain such high mass transport rates, rotation rates of almost 10^6 rpm would be required, which is impossible using the rotating electrode technique. Moreover, the mass transport rate increases proportionally with the reciprocal of the electrode radius. Recently, the RRDE technique has been used to study the orr on carbon-supported Pt nanoparticles to investigate the size effect of catalyst particles on the product distribution during oxygen reduction.^{13–16} The model electrodes used in these studies were prepared by coating a carbon RRDE disk with a Nafion film containing carbon-supported Pt particles. The steady-state diffusion behavior of such electrodes is actually similar to that of a “normal” disk electrode made of platinum in a normal RRDE experiment. Therefore, it is not possible to study the effect of rapid diffusion away from individual particles under steady-state measurements in such model electrode configurations. These studies also suffer from the interference of diffusion through the surrounding Nafion film. In addition, the formation fraction of H_2O_2 may be significantly underestimated in RRDE measurements at the Pt ring electrode because catalytic decomposition of H_2O_2 at this electrode occurs simultaneously and is unseen as a ring current.

It has been suggested that the ideal model electrode system for investigating the size effects of supported electrocatalysts could be produced by deposition of platinum nanocrystals on well-defined substrate surfaces.^{30–32} To obtain catalyst particles of uniform size and shape and to keep particles well separated from each other, the loading of Pt catalyst has to be rather low.^{30–32} For instance, a pulsed electrodeposition method may be used.³¹ However, measurement of the electrocatalytic response of such very low loading electrodes is difficult because of the relatively large background interference from the uncatalyzed substrate. Attempts to increase the Pt loading typically result in a loss of monodispersity and an overlap of adjacent catalyst particles.³⁰ Recently, we have shown that carbon electrodes having very small electroactive areas with effective radii of only a few nanometers may be prepared by electrochemically etching carbon fibers followed by electrophoretic deposition of paint to insulate the body of the etched fibers.³³ With the use of these very small electrodes as substrate, it is possible to limit formation during Pt electrodeposition to only one nucleus during the deposition process, thus forming a single catalyst particle supported on a carbon substrate.³⁴ Such carbon-supported Pt particle electrodes may act as model catalyst particles in the study of fuel cell relevant reactions without the complication of the presence of other nearby catalyst particles allowing measurements under conditions of defined mass transport and kinetics. The effective Pt loading for these electrodes is high even though only a very small catalyst particle is deposited as the electroactive area of the supporting substrate is extremely small. In this paper we conduct a study of the orr in an aqueous acid medium employing such carbon-supported individual Pt particle electrodes. The particle size effects on the reaction pathways and kinetics are explored. It is shown that the catalyst particle size may alter the orr pathway via changing the mass transport rate, even though the particle sizes studied are much larger than those typically used in fuel cell systems. The apparent kinetics of the orr also appear to be affected by the particle size via double-layer effects.

2. Experimental Section

Carbon fibers (PANEX33 CF, 95% carbon, Zoltek Corporation, MO) were used as received, as was the cathodic electro-

phoretic paint solution (Clearclad HSR, LVH Coating Ltd., U.K.). Solutions containing H₂SO₄ (Merck, Aristar), K₂PtCl₄ (Aldrich, 99.9%), Ru(NH₃)₆Cl₃ (Aldrich, 98%), KCl(BDH Analar) were made with Milli-Q water (19 MΩ cm). All experiments are conducted at room temperature. Ultrahigh purity gases were used, with the hydrogen being “CO-free”.

2.1. Electrodes Preparation. *2.1.1. Carbon-Supported Single-Pt-Particle Electrodes.* The preparation of nanometer-sized carbon electrodes has been previously described.^{33,35} The electroactive radii of the prepared carbon electrodes were determined from the steady-state limiting current obtained in 0.01 mol dm⁻³ Ru(NH₃)₆Cl₃ + 0.5 mol dm⁻³ KCl. In this study only the carbon electrodes having effective electroactive radii less than 10 nm are used as substrates to prepare the carbon-supported Pt particle electrodes so that single Pt particles are formed.³⁴ The Pt electrodeposition solution was composed of 0.1 mol dm⁻³ H₂SO₄ + 1 × 10⁻³ mol dm⁻³ H₂PtCl₄. Argon gas was bubbled into the electrodeposition solution for 15 min to remove any oxygen prior to electrodeposition of platinum. During the deposition, an argon atmosphere was maintained above the solution. The Pt was deposited at a constant potential of -0.15 V vs SCE at which potential the deposition process occurs under pure diffusion control.³⁴ The size of the resulting Pt particle was controlled by terminating the deposition either after a specific deposition charge had been consumed or when the magnitude of the current exceeded a predetermined value. Before and after deposition of Pt, the electrodes were rinsed with large amounts of Milli-Q water. SEM images of several typical Pt particle electrodes obtained by this method are shown in refs 34 and 36. In these images it can be seen that the Pt particles sit at the very end of the insulated carbon tips and have an approximately hemispherical shape. These particles are almost uniformly accessible for diffusion of reactants, and the corresponding diffusion geometries around such particles are between hemispherical and spherical. In the following we will assume that the diffusion field around these particle electrodes is uniform. Under such conditions the mass transport coefficient of the electroactive species *i* (*m_i*) on these particles can be defined as^{37,38}

$$m_i = \frac{D_i}{r_{\text{eff}}} \quad (1)$$

where *D_i* is the diffusion coefficient of the corresponding electroactive species and *r_{eff}* is the effective electroactive radius of the catalyst particle. We use the term “effective radius” because the radius values are determined from the steady-state limiting diffusion current by assuming that the particles possess a hemispherical shape. In reality, the particles may not have a perfect hemispherical shape, although as will be shown below such deviations have no effect on our analysis.

These particles are large enough so that their surface can effectively be considered as being composed of polycrystalline, bulk platinum. We do not expect any formation of faceting, or changes in the predominance of different crystal facets with particles size, as has been shown to occur for much smaller particles.³⁹ Indeed, work in the literature suggests that the specific activity of platinum particles due to changes in surface structure does not occur until particles are less than 15 nm in size,⁴⁰ and so we can be confident that the specific activity of our particles and the reaction mechanism remains independent with particle size over the range of particles sizes which we study.

2.1.2. Pt Microdisk Electrodes. Pt microdisk electrodes were made by sealing Pt microwire (12.5 μm radius, Goodfellow

Ltd., Cambridge U.K.) into a tapered glass tube using a resistive heating coil made from Nichrome wire (Advent, Ni80/Cr20, 0.5 mm in diameter). This sealing method can completely seal the metal wires into the glass. The Pt disk was exposed by polishing the electrode on 30 μm alumina paper (Buehler). After the Pt was exposed, the electrodes were then polished with successive grades of alumina paper (9 μm, 1 μm, and 0.3 μm, respectively). Before each use the Pt microdisk electrode was polished with 0.3 μm alumina paper and rinsed in Milli-Q water in an ultrasonic bath. After this, the electrodes were immersed in acidified potassium permanganate solution for 30 min; this treatment was followed by sonication and then a rinse in acidified dilute H₂O₂ solution and then in Milli-Q water.

2.2. Electrochemical Measurement. An AutoLab PG-STAT20 potentiostat with the ECD module (Eco Chemie BV, Netherlands) was used in all electrochemical experiments, and a two-electrode configuration was employed. A calomel reference electrode was employed during electrodeposition of platinum and in the experiments in which the electroactive radii of the carbon electrodes were determined. A large Pt sheet was used as a quasi-reference electrode in the experiments on oxygen reduction and hydrogen oxidation because it is easily cleaned. All potentials are reported with respect to RHE, unless otherwise stated. The glass electrochemical cell and the Pt quasi-reference electrode were immersed in acidified potassium permanganate solution overnight and rinsed with acidified dilute H₂O₂ solution and then Milli-Q water before use.

After rinsing with Milli-Q water, the Pt/carbon electrode assemblies were transferred into the electrochemical cell containing 0.1 mol dm⁻³ H₂SO₄ saturated with high-purity argon and subjected to potential cycling between 0.05 and 1.5 V at a scan rate of 100–500 mV s⁻¹ until a reproducible and well-defined cyclic voltammogram (CV) was obtained. The solution was then replaced by fresh 0.1 mol dm⁻³ H₂SO₄ and oxygenated with high-purity oxygen for at least 15 min. The electrodes were then subjected to several potential scans (0.05–1.5 V) to check the reproducibility of the voltammograms. Immediately after this cycling, a steady-state current–potential curve (1.05 to 0.25 to 1.05 V) was recorded. After measurement on the Pt particle electrodes, steady-state CVs were recorded on two Pt microdisk electrodes in the same solution. The solution was then saturated with research grade CO-free hydrogen by bubbling for 15 min using the same experimental protocol as described above. During the experiments an atmosphere of the corresponding gas was kept in the cell above the solution.

The effective electron-transfer number *n_{eff}* for the orr is calculated from the limiting current *I_L* of the steady-state voltammograms in the presence of oxygen. The steady-state limiting diffusion current obtained on a microelectrode is

$$I_L = B n_{\text{eff}} F D_i c_i^b r_{\text{eff}} \quad (2)$$

where *B* is a factor that depends on the geometric shape of the electrode and *c_i^b* is the bulk concentration of the electroactive species. Glass-sealed Pt microdisk electrodes (25 μm diameter) have a well-defined disk shape, so the values of *D_ic_i^b* can be determined from the limiting current values determined during the steady-state voltammograms of the Pt microdisk electrodes according to eq 2 using *B* = 4, *r_{eff}* = 12.5 μm, *n_{eff}* = 4 for oxygen reduction and *n_{eff}* = 2 for hydrogen oxidation. It is reasonable to assume that *n_{eff}* = 4 for orr on a Pt microdisk electrode of 12.5 μm radius because an electrode of this size has a mass transport rate close to that of a rotating electrode at 4000 rpm, a typical value used in RRDE experiments. Under

such conditions four-electron reduction occurs provided the potential is not within the hydrogen adsorption region. Use of the limiting current from the steady-state CVs obtained on each Pt particle electrode for hydrogen oxidation ($n_{\text{eff}} = 2$) and the known values of $D_{\text{H}_2\text{C}_2\text{H}_2}^{\text{b}}$ determined in the same solutions using the Pt microdisk electrodes of known diameters allows determination of Br_{eff} for that Pt/C catalyst particle. The n_{eff} values for oxygen reduction on each Pt particle can then be determined from the limiting current in the steady-state CV obtained for oxygen reduction according to eq 2, by substituting the values of $D_{\text{O}_2\text{C}_2\text{O}_2}^{\text{b}}$ determined from the CVs of the Pt microdisk electrodes in the same solution and the values of Br_{eff} determined from the CVs for the hydrogen oxidation reaction on the same particle electrodes.

3. Modeling the orr on Single Catalyst Particles

3.1. Current–Potential Behavior. According to the reaction scheme shown in Figure 1, the current density accompanying oxygen reduction can be expressed as

$$j = 4Fv_1 + 2Fv_2 + 2Fv_3 = 4Fk_1\theta_1 + 2Fk_2\theta_1 + 2Fk_3\theta_2 \quad (3)$$

where v_i represents the overall reaction rate of the i th reaction step. θ_1 and θ_2 are the coverage of adsorbed oxygen and hydrogen peroxide species, respectively. Under steady-state conditions we have the following mass balance equations for adsorbed and soluble species

$$\frac{d\theta_1}{dt} = a_1c_{\text{O}_2}^{\text{s}}(1 - \theta) - a_{1-}\theta_1 - k_1\theta_1 - k_2\theta_1 = 0 \quad (4)$$

$$\frac{d\theta_2}{dt} = k_2\theta_1 - k_3\theta_2 + a_2c_{\text{H}_2\text{O}_2}^{\text{s}}(1 - \theta) - a_{2-}\theta_2 = 0 \quad (5)$$

$$\frac{dc_{\text{O}_2}^{\text{s}}}{dt} = D_{\text{O}_2}\left(\frac{dc_{\text{O}_2}^{\text{s}}}{dr}\right) - a_1c_{\text{O}_2}^{\text{s}}(1 - \theta) + a_{1-}\theta_1 = 0 \quad (6)$$

$$\frac{dc_{\text{H}_2\text{O}_2}^{\text{s}}}{dt} = D_{\text{H}_2\text{O}_2}\left(\frac{dc_{\text{H}_2\text{O}_2}^{\text{s}}}{dr}\right) + a_{2-}\theta_2 - a_2c_{\text{H}_2\text{O}_2}^{\text{s}}(1 - \theta) = 0 \quad (7)$$

where θ represents the total surface coverage of all the possible adsorbed species and $1 - \theta$ represents the fraction of surface sites available for adsorption. It is reasonable to assume that the value of $1 - \theta$ stays constant at a defined potential when steady-state has been reached. Thus, we can incorporate the $1 - \theta$ term into the corresponding adsorption rate constant, that is, replace $a_i(1 - \theta)$ with a_i in the above equations. In results, the corresponding adsorption rate constant a_i will depend on the total coverage of adsorbed surface species. The c_i^{s} and $(dc_i/dr)^{\text{s}}$ terms are the concentration and concentration gradient of soluble species i ($i = \text{O}_2$ or H_2O_2) in the vicinity of the electrode surface. The concentration gradients in the vicinity of the electrode can be obtained by solving the steady-state diffusion equations. The solution is given as^{38,41}

$$\left(\frac{dc_i}{dr}\right)^{\text{s}} = \frac{m_i}{D_i}(c_i^{\text{b}} - c_i^{\text{s}}) \quad (8)$$

where m_i is the mass transport coefficient defined in eq 1. Solving eqs 4–8 gives the steady-state values of θ_1 and θ_2 . An expression for the current density is then obtained by substituting the values of θ_1 and θ_2 into eq 3

$$j = \frac{4Fk_1c_{\text{O}_2}^{\text{b}}}{\beta_1} + \frac{2Fk_2c_{\text{O}_2}^{\text{b}}}{\beta_1} + \frac{2Fk_3\beta_2c_{\text{O}_2}^{\text{b}}}{\beta_1} \quad (9)$$

Similarly, if water was the only species produced from the reduction of O_2 then the current density expected would be

$$j_{4e} = 4F\frac{k_1 + k_2}{\beta_1}c_{\text{O}_2}^{\text{b}} \quad (10)$$

Expressions for θ_1 , θ_2 , β_1 , and β_2 are given in Appendix I. Both β_1 and β_2 are functions of the particle size and the reaction rate constants k_i and a_i , which are potential dependent. The current–potential variation can be obtained by substituting the potential dependence of each of the rate constants into eqs 9 and 10.

3.2. Effective Electron-Transfer Number n_{eff} . The effective electron-transfer number accompanying the orr when H_2O_2 is produced and diffuses away from electrodes into solution can be derived from eqs 9 and 10

$$n_{\text{eff}} = \frac{j}{j_{4e}} = 4 - \frac{2}{\left(1 + \frac{k_1}{k_2}\right)(1 + x)} \quad (11)$$

where

$$x = \frac{k_3}{a_{2-}}\left(1 + \frac{a_2}{m_{\text{H}_2\text{O}_2}}\right) = \frac{k_3}{a_{2-}}\left(1 + \frac{a_2r_{\text{eff}}}{D_{\text{H}_2\text{O}_2}}\right) \quad (12)$$

It is clear that the value of n_{eff} will decrease with an increased mass transport coefficient of H_2O_2 , that is, with decreased radius of the catalyst particle when the values of the rate constants involved in eqs 11 and 12 remain constant. It is also implied by eqs 11 and 12 that the mass transport rate-induced change in the value of n_{eff} is significant only when the value of r_{eff} is in a certain range. When the radius of the catalyst particle (r_{eff}) is small enough so that $1 + a_2r_{\text{eff}}/D_{\text{H}_2\text{O}_2} \approx 1$, the n_{eff} value will become almost invariant with r_{eff} and is determined by the value of $(1 + k_1/k_2)(1 + k_3D_{\text{H}_2\text{O}_2}a_{2-})$. When r_{eff} is large enough so that $2/(1 + k_1/k_2)(1 + x) \ll 4$, the value of n_{eff} will be very close to 4 and also independent of the value of r_{eff} , that is, independent of the mass transport rate.

Thus, at certain values of the mass transport coefficient, the value of n_{eff} is determined by the ratio of k_1/k_2 , which represents the competition between the so-called direct four-electron pathway and the series reduction (or indirect) pathway, and the ratio of k_3/a_{2-} , which represents the competition between the electroreduction of adsorbed peroxide species and its desorption. The value of n_{eff} will decrease with the value of these two ratios. Furthermore, n_{eff} will be a function of electrode potential because these rate constants are potential dependent. The detailed relationship between n_{eff} and electrode potential might be a quite complex function that requires knowledge of the dependence of each rate constant on the potential. As well as the rate constant, the potential can affect the surface coverage of various adsorbed species. This will result in a change of the $1 - \theta$ term that for simplicity has been incorporated into a_2 . It can be seen from the above expression of n_{eff} that the effective electron-transfer number accompanying the orr decreases with the value of $1 - \theta$, that is, the adsorption of species other than the reactant or reaction intermediates may result in enhanced formation of hydrogen peroxide.

It should be pointed out that the n_{eff} for the orr can also be affected by the chemical decomposition of H_2O_2 into O_2 and

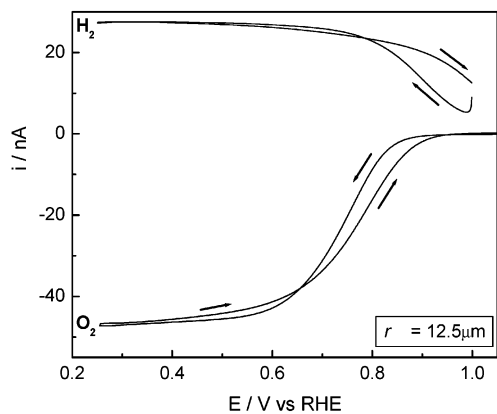


Figure 2. Typical steady-state cyclic voltammograms obtained on a 12.5 μm radius Pt microdisk electrode in either O_2 - or H_2 -containing 0.1 mol dm^{-3} H_2SO_4 solution. (dV/dt): 100 mV s^{-1} .

H_2O without net electron transfer. This paper mainly deals with the effect of the catalyst particle size on the orr reaction mechanism and kinetics. So, we do not include this possible decomposition reaction of H_2O_2 in the reaction scheme and model because this effect would be similar on electrodes of different size. In the above derivations we did not include the concentration of hydrogen ions in the rate equations. Even if the proton is involved in the reaction steps that control the overall reaction rate, the concentration of protons can be considered a constant and included in the rate constants of the corresponding reaction steps. It is also worth mentioning that each reaction step shown in Figure 1 may contain a number of elementary steps. In addition, the reaction intermediates may not necessarily have the exact form as that shown in Figure 1 and might even have multiple forms. However, this will not affect the basic form of the expressions for the current density and n_{eff} . In these alternate cases, the rate constants involved in the above equations have to be replaced by rather more complicated expressions consisting of the rate constants of the elementary steps.

The expression for n_{eff} derived above is not limited to the orr on small particles. It could also be applied to the orr in rotating electrode experiments, but in those cases the mass transport coefficient m_i has to be replaced by $0.620D_i^{2/3}\nu^{-1/6}\omega^{1/2}$. The effect of the rotation rate on the value of n_{eff} might not be seen with rotating electrode techniques as discussed in the Introduction. However, this model may be useful in analyzing the results from rotating electrode experiments investigating the effect of surface blockage, such as oxide formation, hydrogen adsorption, anions adsorption, and so on, on the formation of H_2O_2 during the orr.

4. Results and Discussion

4.1. Particle-Size-Dependent n_{eff} and the Mechanism of orr. Figure 2 shows the typical steady-state cyclic voltammograms obtained on a 12.5 μm radius Pt microdisk electrode for oxygen reduction and hydrogen oxidation. Well-defined limiting current plateau can be found in both $I-E$ curves. The steady-state CVs obtained on two Pt microdisk electrodes of the same diameter are almost identical to each other within an experiment. There was some variation in the limiting current values of the CVs of the Pt microdisk electrodes in different experiments, but this deviation is below 5%. The values of $D_{\text{O}_2}\text{c}_{\text{O}_2}$ and $D_{\text{H}_2}\text{c}_{\text{H}_2}$ determined from these experiments are $(2.41 \pm 0.06) \times 10^{-11}$ mol $\text{cm}^{-1} \text{s}^{-1}$ and $(2.9 \pm 0.1) \times 10^{-11}$ mol $\text{cm}^{-1} \text{s}^{-1}$, respectively. These values compare well to $D_{\text{O}_2}\text{c}_{\text{O}_2} = 2.03 \times$

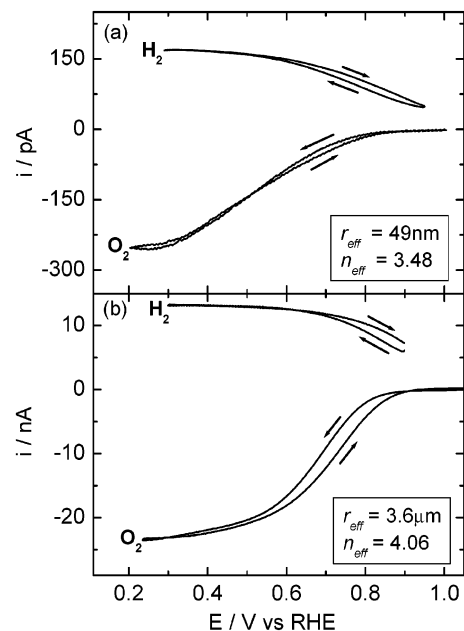


Figure 3. Steady-state cyclic voltammograms obtained on Pt single-particle electrodes of effective electroactive radii of 49 nm (a) and 3.6 μm (b) in either O_2 - or H_2 -containing 0.1 mol dm^{-3} H_2SO_4 solution. (dV/dt): 100 mV s^{-1} . The measured values of the effective electron-transfer number for the orr on each of those particles are displayed in the diagrams.

10^{-11} mol $\text{cm}^{-1} \text{s}^{-1}$ and $D_{\text{H}_2}\text{c}_{\text{H}_2} = 2.24 \times 10^{-11}$ mol $\text{cm}^{-1} \text{s}^{-1}$ calculated from $D_{\text{O}_2} = 1.8 \times 10^{-5}$ $\text{cm}^2 \text{s}^{-1}$ and $\text{c}_{\text{O}_2} = 1.12 \times 10^{-6}$ mol cm^{-3} (both from ref 42) and $D_{\text{H}_2} = 3.8 \times 10^{-5}$ $\text{cm}^2 \text{s}^{-1}$ and $\text{c}_{\text{H}_2} = 0.59 \times 10^{-6}$ mol cm^{-3} (both from ref 43), with the slight variation due to the different conditions under which the measurements were made. For comparison, $D_{\text{H}_2\text{O}_2}$ is 1.45×10^{-5} $\text{cm}^2 \text{s}^{-1}$ under similar conditions.⁴⁴

Figure 3 shows the steady-state cyclic voltammograms obtained on two Pt particle electrodes of different radii. The CVs obtained on larger particles are very similar to that in Figure 2. On small particles, however, the CVs for the oxygen reduction reaction are obviously drawn out because of the irreversibility of the orr under accelerated mass transport. The limiting current value is still readable from the negative limit of the CVs when r_{eff} is larger than 50 nm. It is more difficult to get CVs for oxygen reduction having well-defined limiting currents when the effective radii of particles is smaller than this value, as these limiting currents do not occur until within the hydrogen adsorption region.

It can be seen that for these steady-state CVs the orr current on the positive-going $I-E$ curves are always larger than those on the negative-going scans. This is a common characteristic for steady-state CVs for oxygen reduction and has also been obtained on bulk Pt electrodes while using rotating electrode techniques. The orr activity is always higher during the positive-going scan because of the orr taking place on an oxide-free surface. The numbers inserted in Figure 3 indicate the values of the effective electron-transfer number calculated from the limiting current values using eq 2. On the larger particle electrode (3.6 μm effective Pt particle radius), the value of n_{eff} is close to 4, whereas the calculated n_{eff} value is about 3.5 at the Pt particle of effective radius of ~ 50 nm.

Figure 4 shows the variation of n_{eff} at a potential of 0.4 V (RHE), that is, within the double-layer region, with the effective radius of the Pt particle (r_{eff}) obtained from the steady-state CVs on electrodes having a range of particle sizes. This potential was chosen because it is outside the hydrogen adsorption region

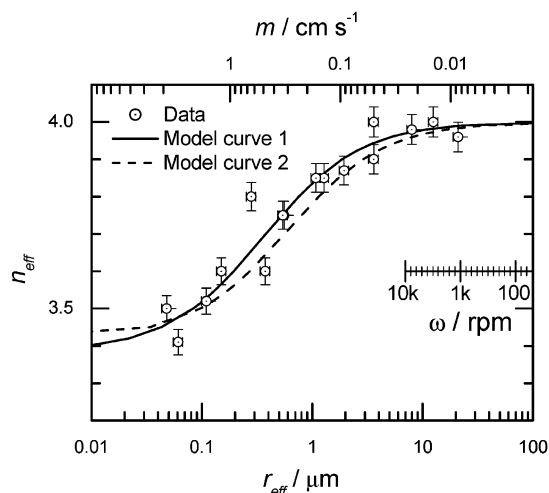


Figure 4. Variation of the value of n_{eff} with the effective radius of single carbon-supported Pt particles for the orr at 0.4 V (RHE) in O_2 -saturated 0.1 mol dm^{-3} H_2SO_4 . The lines represent simulations of the curves using eq 11 utilizing the following parameters: $k_1/k_2 = 1.0$, $k_3/a_{2-} = 0.72$, $a_{2-} = 0.4$ (solid curve); $k_1/k_2 = 0.0$, $k_3/a_{2-} = 2.2$, $a_{2-} = 0.4$ (dashed curve), respectively. The top x -scale shows the equivalent mass transport coefficient assuming a diffusion coefficient of $1.6 \times 10^{-5} \text{ cm}^2 \text{ s}^{-1}$, a value intermediate between that of hydrogen peroxide and oxygen. Set within the figure is an indication of the equivalent rotation rates required to achieve the same mass transport conditions utilizing a rotating electrode in aqueous electrolyte.

but provides a point at which a limiting current is seen on the smallest Pt particles examined. If a higher potential is used, the diagram is exactly the same as that shown in Figure 4 except for the exclusion of points from the smallest electrodes, as these do not show a limiting current at that higher potential. Thus, the reason for choosing the lower potential is to provide the widest range of accessible mass transport rates, and the conclusions drawn from the plots are generally applicable to oxygen reduction at any potential above the hydrogen adsorption region.

The top x -scale in Figure 4 corresponds to the mass transport coefficient at the equivalent electrode radius assuming a diffusion coefficient of $1.6 \times 10^{-5} \text{ cm}^2 \text{ s}^{-1}$, that is, a value intermediate between those of oxygen and hydrogen peroxide. Also displayed in Figure 4 is a scale representing the equivalent disk rotation rates under the same conditions. It can be seen that the value of n_{eff} shows a continuous decrease with r_{eff} in the range from 3 micrometers down to 100 nanometers. When the radii of particles are below 100 nm, the decrease of n_{eff} becomes less obvious, although the value of n_{eff} appears to start leveling out at a value less than 3.5. An n_{eff} value of 3.5 corresponds to a situation in which 75% of oxygen molecules are reduced to water and 25% are reduced to H_2O_2 . As mentioned above, measurement of the n_{eff} values on particles smaller than about 50 nm is problematic, as the limiting oxygen reduction current does not occur until the hydrogen adsorption region, and as has already been discussed, we expect there to be enhanced H_2O_2 production within that potential range. According to eq 11 and considering that $1 + k_3/a_{2-}$ is always larger than 1, the value of k_1/k_2 has to be less than 2.5 to allow such small n_{eff} values to occur. Obtaining more accurate values is difficult although we find reasonable fits to the data with restricted sets of parameters. A reasonable fit to the whole set of data in Figure 4 with the model equations can only be achieved by setting $k_1/k_2 < 1.5$ and a_2 to 0.4. Two fitting curves are shown in Figure 4 using the following parameters values: $k_1/k_2 = 1$, $k_3/a_{2-} = 0.72$, $a_2 = 0.4 \text{ cm s}^{-1}$ and $k_1/k_2 = 0$, k_3/a_{2-}

$= 2.2$, $a_2 = 0.4 \text{ cm s}^{-1}$, respectively. In all cases, a $D_{\text{H}_2\text{O}_2}$ of $1.45 \times 10^{-5} \text{ cm}^2 \text{ s}^{-1}$ was used.⁴⁴

From the experimental data and the model curves, it is clear that the variation of n_{eff} mainly occurs on particle having sizes ranging from 50 nm to 5 μm . On particles larger than 5 μm , the n_{eff} value is larger than 3.97 and hardly changes with the particle size, that is, the fraction of hydrogen peroxide produced is less than about 2%. This is in good agreement with the conclusion obtained from the RRDE measurements on large electrodes. When the radius of particles is less than 50 nm, the value of n_{eff} appears to also tend toward a constant. This is because the diffusion of H_2O_2 is so rapid at small particles that the local concentration of H_2O_2 adjacent to the electrode is effectively zero and the rate of loss of H_2O_2 is controlled by the a_{2-} desorption process. Thus, the formation rate of H_2O_2 is mainly governed by the competition between the so-called direct four-electron pathway and the series or indirect pathway (k_1/k_2) and the competition between the electroreduction steps of reaction intermediates $\text{H}_2\text{O}_{2\text{ad}}$ and its desorption steps. The Pt particles used in fuel cell catalytic electrodes usually have radii less than 5 nm. The data and the model curves in Figure 4 indicate that changes in particle size over this range should have little effect on the formation fraction of hydrogen peroxide resulting from the mass transport effect. Of course, other effects at such small particles, for instance, variations in the prevalence of different crystallite facets, may play an important part in the reactions occurring.

Another aspect which will have a significant effect in real fuel cell systems is the fact that other particles will exist in close proximity to each other. They will tend to form diffusion spheres that collide and interact to greater or lesser extent depending upon the interparticle separation and diffusion coefficient of the reactant. The net effect will be to lower the local mass transport coefficient. The extent to which this occurs will be highly geometry dependent. Indeed, in agreement with our work, Watanaba et al.²³ have suggested that a large separation between adjacent particles should be able to increase the overall oxygen reduction activity on supported Pt nanoparticles. In other words, not only the particle size but the Pt loading plays a key role in determining the specific mass activity of the carbon-supported Pt particle electrodes toward oxygen reduction.

Another interesting conclusion obtained from examining the fitting curves for Figure 4 is that our results do not exclude a pure series (i.e., indirect) reaction mechanism for oxygen reduction on Pt electrodes in sulfuric acid solution, that is, exclusively following the lower branch in Figure 1. When $k_1/k_2 = 0$, the model curve still well fits the experimental data. Within Figure 4 we see that, even for the pure series mechanism, approximate four-electron reduction of oxygen occurs provided the particle is not very small, for example, provided it is $> 5 \mu\text{m}$ in size. The corresponding mass transport coefficient is about 0.04 cm s^{-1} , equivalent to a rotation rate of about 25 000 rpm. Thus, our present study shows that the series pathway (i.e., indirect hydrogen peroxide pathway) plays an important role in the orr, rather than a negligible role as generally believed. Within the general electrochemistry literature, the conclusion that the direct four-electron reduction pathway is the predominant pathway in orr on Pt is generally based on several facts obtained in RRDE experiments. For instance, little ring current due to the oxidation of peroxide is generally detected^{4–10,12–15} and pronounced formation of H_2O_2 is only observed when strongly adsorbed surface species are present, for example, strongly adsorbed anions such as Br^- , Cl^- , and so on^{1,2,7,9–12,15} or some surface UPD (underpotential deposition) atoms such

as H, Pb, Cu, and so on.^{2,7,8,10–12,45–49} It is shown in the present study that the small values of ring current may be due to the low mass transport rate accessible using typical RRDE experiments. Under such mass transport conditions, the nearly complete four-electron reduction is possible following the pure series (indirect) mechanism. The effect of a blocking species on the formation of H₂O₂ has been generally attributed to the inhibition of the dissociative adsorption of the oxygen molecule on the Pt surface, a process that is considered to be the initial step of the direct four-electron reduction pathway. Thus, the increased rate of H₂O₂ production in the presence of strongly adsorbed species has been considered as being indirect evidence of the direct four-electron reduction pathway.^{1,2} However, the enhancement of H₂O₂ formation induced by surface adsorption of spectator species might not be a unique indicator for the direct pathway reaction mechanism. If we set $k_1/k_2 = 0$ and separate the $1 - \theta$ term from the adsorption rate constant, the expression for n_{eff} then becomes

$$n_{\text{eff}} = 4 - \frac{2}{1 + \frac{k_3}{a_{2-}} \left[1 + \frac{a_2(1 - \theta)}{m_{\text{H}_2\text{O}_2}} \right]} \quad (13)$$

It is very clear that a decrease in the value of $1 - \theta$ will result in a decline in the n_{eff} value when the mass transport coefficient and rate constants are invariant. This indicates that surface blockage by the strongly adsorbed species can significantly increase the formation fraction of H₂O₂ during oxygen reduction while exclusively following the pure series (indirect) mechanism. In studies of the orr on Pt low-index single-crystal faces in aqueous acid solution by Markovic et al.,^{7,11} it was found that O₂ almost completely undergoes a two-electron reduction to H₂O₂ on a Pt(111) electrode in the H UPD region. Separate experiments in oxygen-free H₂O₂-containing solution showed that the reduction of H₂O₂ is almost totally inhibited in this potential region on the Pt(111) electrode. The authors believed that the two experiments confirmed the speculation that the pronounced formation of H₂O₂ induced by adsorption of blocking species is due to a loss of surface sites for the O–O bond cleavage that is the initial step of the direct four-electron reduction pathway. It seems to us that a counter argument could be made that the hydrogen peroxide pathway plays an important role in the oxygen reduction reaction (i.e., that the indirect pathway in Figure 1 is the dominant pathway). In our approach, we would argue that the adsorption equilibrium of hydrogen peroxide involved in the series (indirect) pathway of the orr is probably also the initial step in the reduction of H₂O₂. The adsorption of hydrogen can inhibit the H₂O₂ adsorption step and favors the desorption of the peroxide species. This might be the common reason for the enhanced formation of hydrogen peroxide accompanying orr and the inhibition of H₂O₂ reduction in the H UPD region. In contrast, if a pronounced rate of H₂O₂ formation occurs during the orr in the presence of strong surface adsorption while the reduction of H₂O₂ is not obviously inhibited under the same conditions, one may conclude that the hydrogen peroxide pathway plays a minor role in the O₂ reduction reaction; yet this case is not observed.

4.2. Kinetics of Oxygen Reduction on Carbon-Supported Pt Single Particles. The kinetics of the orr is generally analyzed using a Tafel relationship between the current and potential. Frequently, two slopes can be found in Tafel plots obtained during the orr on Pt. In the low-potential region (generally called the high current density region or high-overpotential region), a Tafel slope of around -120 mV per decade of current density

occurs, which has been explained as a rate-determining first electron-transfer process for which the corresponding transfer coefficient is close to 0.5.^{1,5,7–12,18–20} The slopes of Tafel curves in the high-potential region (low current density region) are typically around -60 mV per decade of current density on Pt electrodes in pure sulfuric or perchloric acid solutions. A transition in slope occurs at potentials between 0.8 and 0.85 V. Such changes in slope of the Tafel plots for the orr have been attributed to a change of the adsorption mode of the reactant and reaction intermediates on the electrode surface, for example, from Langmuirian adsorption to Temkin adsorption,^{5,18–20} or has been explained in terms of the potential-dependent coverage of surface oxide like PtOH which inhibits the adsorption of O₂ and reaction intermediates.^{1,2,7–12,50–52} The inhibitory mechanism seems to be more reasonable and has been supported by some indirect evidence.^{1,2,7–12} Such inhibition effects of surface oxide on the rate of oxygen reduction can be shown by expressions for the apparent rate constant k_{app} of orr, that is

$$k_{\text{app}} = k^0(1 - \theta) \exp\left[\frac{-\alpha F(E - E^0)}{RT}\right] \exp\left(\frac{-\Delta G_\theta}{RT}\right) \quad (14)$$

This equation is straightforwardly derived from eq A9 (shown in Appendix II) by replacing the adsorption equilibrium constant a_1/a_{1-} with its equivalent in terms of the adsorption free energy ΔG_θ and separating the $1 - \theta$ term from a_1 . It can be seen that the surface oxide may affect the reaction rate in two ways. First, it reduces the number of surface sites available for oxygen adsorption, that is, decreases the value of $1 - \theta$. Second, it modifies the free energy for oxygen adsorption. Furthermore, not only the surface oxide but also other surface-adsorbed species may affect the orr rate in a similar way and can thus be described using eq 14. Such a rate equation has been used by Markovic et al.^{2,9} for oxygen reduction on Pt single-crystal electrodes. This expression is different from that given by Damjanovic et al.^{18–20} in which the $1 - \theta$ term is not included. The slopes of the Tafel plots depend on the value of the transfer coefficient α of the first electron-transfer step, the potential dependence of the total coverage of all adsorbed species, and the potential dependence of ΔG_θ , the latter depending on the interaction between neighboring adsorbed species. It should be pointed out that eq 14 is only valid when the electron-transfer step is very slow compared to the adsorption step, that is, the electron transfer between the electrode and the adsorbed reactant determines the overall reaction rate and the surface coverage of oxygen is approximately determined by the adsorption/desorption equilibrium. This is more likely the case at low overpotentials. At very high overpotential, the electron-transfer step may become rather rapid and is thus no longer the slowest step in the overall reaction pathway. Thus, the reaction becomes diffusion or adsorption controlled. In most of the kinetics studies of the orr by rotating electrode techniques, mixed kinetic/diffusion control is mostly observed at potentials above 0.7 V in sulfuric or perchloric acid solution. At lower potentials limiting diffusion behavior usually occurs. In the present study we use single-particle electrodes having effective radii down to the submicrometer scale. The rapid mass transport at such small particles can compensate for reactant consumption so that a higher overpotential is required to reach limiting diffusion conditions. Figure 5 shows a series of steady-state polarization curves for oxygen reduction on Pt particles of different sizes. A number of interesting features are obvious from this plot. The first is that, as the particle size is decreased, the current density for oxygen reduction increases, as might be expected from the increased mass transport coefficient of the smaller

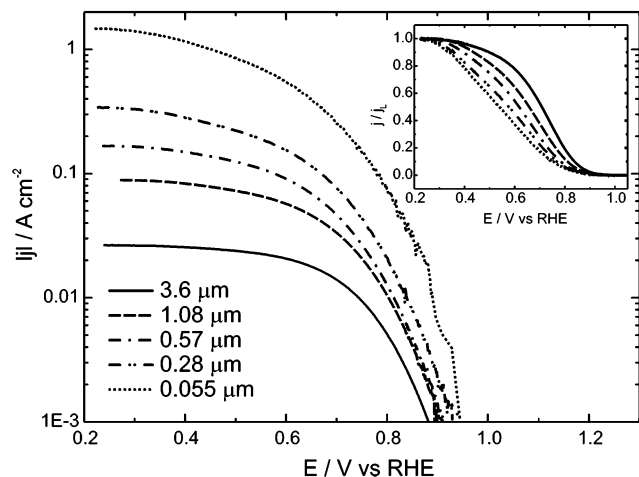


Figure 5. Steady-state $|j|$ – E profiles obtained during positive-going scans for the orr in O_2 -saturated $0.1 \text{ mol dm}^{-3} \text{ H}_2\text{SO}_4$ on carbon-supported Pt particle electrodes. Inset: Data in the main figure normalized by the corresponding limiting j values at the negative potential limit. The numbers in the figure indicate the radii of Pt particles. Scan rate: 100 mV s^{-1} .

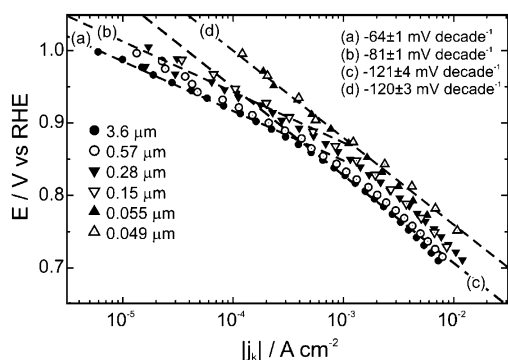


Figure 6. Tafel plots of the kinetic current in the potential region above 0.7 V obtained from the steady-state I – E curves for the orr in $0.1 \text{ mol dm}^{-3} \text{ H}_2\text{SO}_4$ on Pt single-particle electrodes. The radii of the particles and the slope of the fitted Tafel lines are indicated in the figure.

electrodes. It is interesting to see that these effects are present even at potentials as high as 0.95 V indicating that mass transport effects still have a significant effect on catalyst performance at such high potentials. The increased current density seen on the smaller Pt particles at high potentials at which mixed kinetic and mass transport control exists suggests that poisoning or deactivation of the catalyst surface is not significant and should have no effect on the validity of the results presented in this paper.

Inset into Figure 5 are the normalized steady-state I – E profiles of the data provided in the main diagram. The current is normalized to the corresponding limiting value at the negative potential limit. It can be seen that the steady-state I – E curves obtained at relatively large particles (e.g., $r_{\text{eff}} > 1 \mu\text{m}$) have well-defined S shapes. The I – E curve becomes gradually less reversible with decreased particle size, and the limiting diffusion behavior occurs at a more negative potential. This enables us to investigate the kinetics of the orr within the higher overpotential regions.

4.2.1. Tafel Plots. The Tafel plots for the kinetic current density (j_k) of the orr obtained on a set of particle electrodes are given in Figure 6 and Figure 7 for different potential regions. The j_k values are determined from the measured current density j and the limiting diffusion current density j_L on the steady-state I – E curves using eq A7. The effective active area of the particle electrodes is determined from the charge involved in

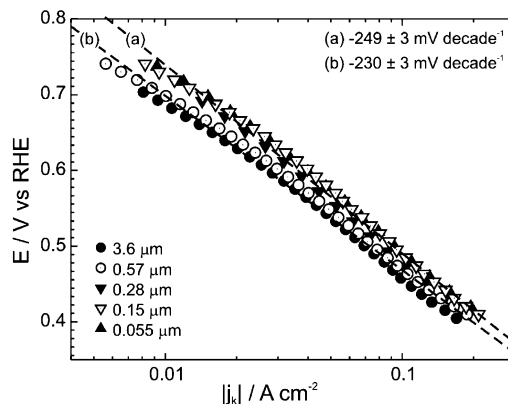


Figure 7. Tafel plots of the kinetic current in the potential region between 0.4 V and 0.7 V obtained from the steady-state I – E curves for the orr in $0.1 \text{ mol dm}^{-3} \text{ H}_2\text{SO}_4$ on Pt single-particle electrodes. The radii of the particles and the slope of the fitted Tafel lines are indicated in the figure.

the hydrogen adsorption–desorption process in CVs obtained in oxygen-free $0.1 \text{ mol dm}^{-3} \text{ H}_2\text{SO}_4$. The current density values are those obtained from the steady-state I – E curves obtained during the positive-going scan where the reaction takes place on a prerduced electrode surface.

It can be seen from Figures 6 and 7 that the Tafel curves obtained on particles of different size have similar slopes to each other in the potential range below 0.85 V although the kinetic current density is slightly larger on smaller particles. For example, the kinetic current density obtained at particles having radii around 50 nm is about 1.5 times larger than those obtained on particles having radii larger than 500 nm when the potential is below 0.85 V . The Tafel curves obtain at particles larger than 500 nm almost overlap each other once the potential is below 0.85 V . In general, a slope of around -120 mV per decade can be fitted to the Tafel plots over the potential region between 0.85 and 0.75 V , as shown by the lines c and d in Figure 6. The Tafel plots in the potential region above 0.85 V obtained on particles having radii larger than 500 nm have low values of slope close to -60 mV per decade of current density, as indicated by line a. This indicates that the Tafel behavior of these large particles is identical to that on bulk Pt electrodes. However, as the radius of the Pt particle becomes smaller than 500 nm , the slope of the Tafel plots in this high-potential region shows a general increase with decreasing particle size. In these results only one single slope of -120 mV per decade can be found for the Tafel curves at particles having an effective radius of less than or equal to 55 nm over the entire potential region above 0.7 V (line d in Figure 6). This single Tafel slope behavior is different to that reported by Markovic et al.^{2,7–9,11} for the orr on Pt(111) single-crystal electrodes in bisulfate- or halide-ion-containing media. In their studies, the single-slope behavior on Pt(111) electrodes is always accompanied by significant inhibition of the orr, which was attributed to the loss of surface sites for both oxygen and its reduction intermediates due to anion adsorption. No inhibition of the orr occurs at the smallest electrodes which we studied even though they show a single slope. Indeed, we see an enhanced kinetic current density at smaller particles. The authors explained the single Tafel slope behavior in terms of a delay in PtOH formation due to strong adsorption of anions on the Pt(111) surface.^{2,7} The formation of PtOH on this crystal plane occurs only when the potential is more positive than 1.0 V in bisulfate-containing solution. So, it is expected that the Tafel slope of -120 mV covers the entire potential region below 1.0 V . As the oxygen reduction process

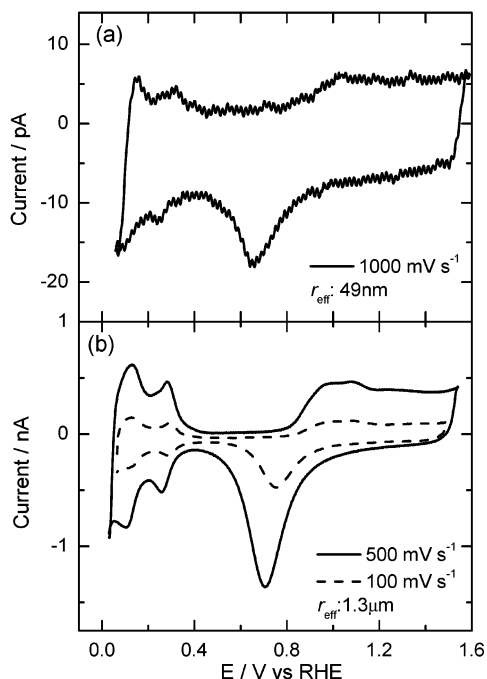


Figure 8. Cyclic voltammograms obtained on electrodes of carbon-supported single Pt particles in 0.1 mol dm⁻³ H₂SO₄ saturated with high-purity Ar. The effective radii of the particles are 49 nm (a) and 1.3 μm (b), respectively.

is strongly inhibited by anion adsorption, the corresponding reduction current is too low to conduct kinetic analysis in the positive potential region (low-overpotential region); thus, the Tafel behavior for the orr on Pt(111) electrodes in 0.05 mol dm⁻³ H₂SO₄ seems only to extend as far positive as 0.85 V rather than the entire region of $E < 1.0$ V.^{7,11,12} In fact, the Tafel plots obtained on the other two low-index single-crystal electrodes Pt(100) and Pt(110) also have a single slope of approximately -120 mV per decade over the entire potential region below 0.85 V.⁷ In another research paper by Markovic et al. dealing with the effect of Br⁻ addition on the orr on Pt(111) in 0.1M HClO₄, it was reported that the Tafel slope changes from -76 to -118 mV per decade as the amount of Br⁻ is increased.⁷ However, the Tafel plots shown for the solution with and without Br⁻ are in totally different potential regions. The Tafel plot for pure 0.1M HClO₄ is in the range of 0.4–0.6 V vs SCE, whereas for the Br⁻-containing solution it is below 0.4 V where in bromide-free HClO₄ the Tafel slope would be expected to be close to -120 mV per decade. Thus, it seems that there is no direct correlation between the single-slope behavior on Pt(111) with the delay of surface oxide formation. Instead, the single Tafel slope behavior might be due to the significant depression of reduction current in the high-potential region where the low Tafel slopes occur. As shown in Figure 6, the single Tafel slope of approximately -120 mV per decade extends to the potential region above 1.0 V for the orr on small particles. However, no obvious delay in oxide formation can be seen on these small particles, as shown in the CVs for different-sized particles in Ar-saturated 0.1 mol dm⁻³ H₂SO₄ (Figure 8).

So, it would appear that in our system increased Tafel slopes in the high-potential region are not directly linked to a delay of the formation of surface oxide (or adsorption of OH). This seems to imply that the transition in Tafel slopes is not necessarily due to surface oxide formation. Instead, we propose an alternative mechanism below.

In the low-potential region from 0.4 to 0.7 V, we observe Tafel slopes on these small particles of around -240 mV per decade (Figure 7). According to eq 14, deviation of the Tafel slope from -120 mV per decade may be due to a potential dependence of the $1 - \theta$ term or of the adsorption energy. Indeed, both of these parameters are affected by the potential-dependent change of the total surface coverage of adsorbed species. In this potential region the main adsorbed species may be anions as the electrode surface is free of surface oxide. Because the anion coverage should increase with increasing potential in this region, it is expected that the Tafel slope would be less than the -120 mV per decade as seen in the oxide region. Such large Tafel slopes might be due to the rate-determining step for the orr being different from that in the potential region above 0.7 V. For instance, the initial adsorption of oxygen becomes the rate-determining step at high overpotential where the electron-transfer step becomes rather fast so that the rate equation changes from eq A9 to A10. The slope of -240 mV per decade indicates an apparent value of 0.25 for the symmetry factor. This value could result from a coupling between the potential dependence of the bisulfate coverage and a potential dependence of the adsorption rate constant a_1 . As will be discussed below, such a low transfer coefficient value might also be related to a double-layer effect.

The exchange current density j^0 can be obtained by extrapolating the Tafel line. Two sets of j^0 values can be obtained from the Tafel plots in the potential region where the reaction rate is determined by the electron-transfer step. Only one set of j^0 values can be obtained from the Tafel plots obtained on Pt particles of 50 nm radius or less because those Tafel plots only show a single slope. From the j^0 values, the apparent values of the standard rate constant can be determined using

$$j^0 = 4Fk_{\text{app}}^0 c_{\text{O}_2}^b \quad (15)$$

The results are listed in Table 1.

4.2.2. Particle-Size-Dependent Half-Wave Potential. As shown in Figure 5, the electrode reaction becomes more irreversible as the particle size decreases. Furthermore, the half-wave potential ($E_{1/2}$, the potential at which the current reaches half the value of the limiting diffusion current) in the steady-state I - E curves shifts toward lower potentials (i.e., higher overpotentials). Figure 9 summarizes the size dependence of the half-wave potential values obtained from the steady-state I - E curves for the orr obtained in our experiments. It can be seen that there is a reasonable linear relationship between the values of $E_{1/2}$ and the values of $\log(r_{\text{eff}})$. The fitted line has a slope of 119 ± 11 mV per decade of r_{eff} .

A theoretical relationship between $E_{1/2}$ and r_{eff} is straightforward from the relationship between the current and the particle size, that is, eq A5. Setting $j = 1/2 j_L$, we have

$$k_{1/2,\text{app}} = m_{\text{O}_2} \quad (16)$$

where $k_{1/2,\text{app}}$ is the rate constant at the half-wave potential, that is, $E = E_{1/2}$. Substituting $m_{\text{O}_2} = D_{\text{O}_2}/r_{\text{eff}}$ and eq A8 into eq 16 leads to

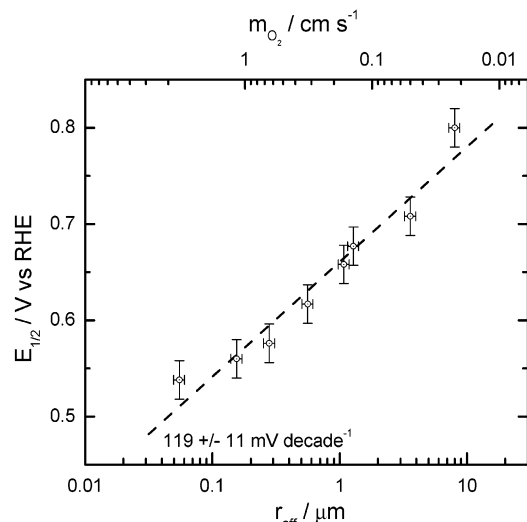
$$E_{1/2} = E^0 + \frac{RT}{\alpha F} \ln \left(\frac{k_{\text{app}}^0 r_{\text{eff}}}{D_{\text{O}_2}} \right) \quad (17)$$

The significance of the symbols in this equation are given in Appendix II. A similar expression to eq 17 has been given by Oldham et al. for a simple redox reaction at a hemispherical

TABLE 1: Apparent Values of the Standard Rate Constant k_{app}^0 and Exchange Current Density j^0 Extracted from the Steady-state $I-E$ Profiles of the Oxygen Reduction Reaction in $0.1 \text{ mol dm}^{-3} \text{ H}_2\text{SO}_4$ on Electrodes of Single Pt Particles of Different Size

$r_{\text{eff}} (\mu\text{m})$	$k_{\text{app}}^0/\text{cm s}^{-1}$			$j^0/\text{A cm}^{-2}$		
	Tafel plot ^a	Tafel plot ^b	half-wave ^c	Tafel plot ^a	Tafel plot ^b	half-wave ^c
3.60	1.2×10^{-6}	5.5×10^{-9}	2.2×10^{-6}	5.0×10^{-7}	2.4×10^{-9}	1.0×10^{-6}
0.56	1.3×10^{-6}	6.5×10^{-9}	2.4×10^{-6}	5.6×10^{-7}	2.8×10^{-9}	1.0×10^{-6}
0.28	2.5×10^{-6}	1.8×10^{-8}	2.3×10^{-6}	1.1×10^{-6}	8.0×10^{-9}	1.0×10^{-6}
0.15	2.7×10^{-6}	1.4×10^{-7}	3.0×10^{-6}	1.2×10^{-6}	6.5×10^{-8}	1.3×10^{-6}
0.05	3.7×10^{-6}	3.7×10^{-6}	5.6×10^{-6}	1.6×10^{-6}	1.6×10^{-6}	2.4×10^{-6}

^a From Tafel plots of 120 mV slope region. ^b From Tafel plots of 60 mV region. ^c From half-wave potential values.

**Figure 9.** Variation of the value of the half-wave potential for the steady-state $j-E$ curve (Figure 5, inset) with particle size during the orr in $0.1 \text{ mol dm}^{-3} \text{ H}_2\text{SO}_4$ at Pt single-particle electrodes.

microelectrode.⁵³ To obtain eq 17, an assumption that the apparent reaction rate constant k of the four-electron oxygen reduction has a Butler–Volmer type dependence on the potential E has to be made (see Appendix II). The linear relationship between $E_{1/2}$ and $\log(r_{\text{eff}})$ shown in Figure 9 indicates that this assumption is reasonable.

The 119 mV per decade slope of the $E_{1/2} \sim \log(r_{\text{eff}})$ plot indicates that the apparent transfer coefficient α is close to 0.5, which is similar to the transfer coefficient values usually obtained from the Tafel plots of oxygen reduction in the high current density region (when $E < 0.85 \text{ V}$). From eq 17, the apparent standard rate constant (k_{app}^0) can be determined using $E^0 = 1.23 \text{ V}$; therefore, the exchange current density j^0 can be determined using eq 15. The values of k_{app}^0 and j^0 calculated in this way are given in Table 1.

4.2.3. Kinetic Parameters. Table 1 gives the values of the apparent standard rate constant k_{app}^0 and the exchange current density determined using the Tafel method and half-wave potential method, respectively. On particles having effective radii larger than 500 nm, the j^0 values determined from the Tafel plots in the low current density region (approximately -70 mV per decade slope region) are around $2.5 \times 10^{-9} \text{ A cm}^{-2}$ (corresponding to k_{app}^0 values of around $6 \times 10^{-9} \text{ cm s}^{-1}$). Such values are close to those normally obtained on bulk Pt electrodes in sulfuric acid solutions.^{18–20} The j^0 and k_{app}^0 values evaluated from the Tafel plots in this potential region increase significantly upon decreasing the particle size once r_{eff} becomes less than 500 nm. This is because of the slope of the Tafel plots in this potential region becoming larger on smaller particle, as shown in Figure 6. Although the values of j^0 and k_{app}^0 extrapolated from the Tafel plots in the low-potential region (high current

density region) in Figure 6 also show some variation at $r_{\text{eff}} < 500 \text{ nm}$, this change is much less than that seen in the high-potential region. The values calculated for j^0 in this potential region are mostly around $1 \times 10^{-6} \text{ A cm}^{-2}$ and increase slightly with decreasing particle size. It can be seen that the values of k_{app}^0 and j^0 obtained from the half-wave potential method are very close to those obtained from the Tafel plots in the low-potential region where slopes of around -120 mV per decade of current density occur. In addition, both the slope of the Tafel plots in the low-potential region and the slope of the $E_{1/2} \sim \log(r_{\text{eff}})$ give an apparent transfer coefficient (α) value of about 0.5. This implies that the same kinetic processes are behind these two measurements. For a simple redox process this would be easy to understand as both the Tafel relationship and the $E_{1/2} \sim \log(r_{\text{eff}})$ relationship are derived from the expression relating the current density to the particle size, that is, eq A5. But the orr is a multistep reaction involving surface adsorption of a reactant and reaction intermediates. The overall reaction rate constant is a complex expression of the electron-transfer rate constant and adsorption rate constant, for example, eq A6. Even when the electron-transfer step is the rate-determining step, the potential dependence of the apparent rate constant is affected by surface adsorption, for example, eq A9. Because surface adsorption varies with potential, the reaction rate should show a variation in its potential dependence within the different potential region as indicated by changes in the slope of the Tafel plots. The $E_{1/2}$ values determined from the steady-state polarization curves occur mostly below 0.8 V (Figure 9) where the Tafel plots in Figure 6 have a slope of about -120 mV per decade. So, the kinetics revealed by the $E_{1/2} \sim r_{\text{eff}}$ relationship is similar to that behind the Tafel behavior in the -120 mV per decade region. When the $E_{1/2}$ point occurs at potentials above 0.85 V, we expect that the kinetic constants determined from the $E_{1/2} \sim r_{\text{eff}}$ plot would be close to those extrapolated from the 60 mV per decade Tafel plots. In order for $E_{1/2} > 0.85 \text{ V}$ we require that the radius of the particle is larger than 50 μm according to eq 17. In reality, the radius of the particle has to be larger than 1.5 mm since the slope of the $E_{1/2} \sim \log(r_{\text{eff}})$ would be 60 mV instead of 120 mV in the potential region above 0.85 V. On such large electrodes, steady-state measurement is impossible under stationary electrode conditions.

The kinetics parameters obtained from the Tafel plots with -120 mV per decade slopes and those obtained from the particle-size-dependent half-wave potentials should represent the real kinetics of the orr governed by the electron-transfer step since they exclude any possible interference from surface oxide. The Tafel plots with -60 mV per decade slopes provide information about the orr influenced by the presence of oxide, which modifies the transfer coefficient and the reaction rate constant via changing the effective surface site availability and the free energy of adsorption. In fact, even the kinetic parameters estimated from the half-wave potentials and the Tafel plots with -120 mV per decade slope are not the real kinetics of the orr

on Pt electrodes, as these results are affected by the adsorption of anions such as bisulfate. The real kinetic parameters for the orr on bare Pt electrodes may be obtained under conditions where no anion adsorption occurs, for example at the Pt/Nafion membrane interface. The -120 mV per decade slope of the Tafel plots and 120 mV per decade slope of the $E_{1/2} \sim \log(r_{\text{eff}})$ line suggest that the rate-determining step is a one-electron transfer with $\alpha \approx 0.5$, seemingly indicating that the orr kinetics is not affected by the adsorption of anions. Slopes close to -120 mV per decade in the high current density region have also been observed on Pt single-crystal electrodes in halide-ion-containing solution.^{7–12} The authors of that work believed that the adsorption of halide ions would only affect the $1 - \theta$ term and not the free energy of oxygen adsorption (ΔG_θ). However, it is rather hard to accept that the adsorption of OH affects the free energy of oxygen adsorption but that the adsorption of anions does not. The most likely reason for the observed almost pure electron-transfer kinetics in this potential region might be that the adsorption of anions reaches saturation coverage and then changes little with potential. Thus, both the term $1 - \theta$ and ΔG_θ remain approximately constant over this potential region. Under such conditions, the measured transfer coefficient value would be that of the pure electron-transfer reaction. In our experiments, the k_{app}^0 measured is the rate constant of electron-transfer reaction modified by the $1 - \theta$ and $\exp(-\Delta G_\theta/RT)$ terms. The role of anion adsorption may be much more complicated than simply that of surface blockage, as will be discussed in the next section.

The kinetics analysis and discussion addressed above are all based on the assumption that any oxygen is fully reduced to water. The effects of hydrogen peroxide formation are ignored. This is because the effect of hydrogen peroxide formation on the current density is rather small. Even at very small electrodes, the current density deviation due to hydrogen peroxide formation is only $\sim 10\%$. At larger particle electrodes, this deviation is much less. The correction to the current density in considering the formation of hydrogen peroxide results in only negligible changes to the Tafel slopes and exchange current density values. At small particle electrodes, the reaction is highly irreversible and the limiting current density is much larger than the kinetic current density over virtually the entire potential range so that $1/j_K \gg 1/j_L$, and the latter parameter may be ignored in the kinetic equations.

4.2.4. Possible Effects of the Electric Double Layer on the orr Kinetics on Single Catalyst Particles. The activation energy barrier for the electron-transfer process in an electrochemical reaction is overcome by the potential difference between the electrode and the electrolyte solution, as indicated in the exponential term of the Butler–Volmer equation.^{54,55} This potential difference distributes itself in the electric double layer formed at the electrode/electrolyte interface. It has been long realized that the location of the electron-transfer site in the double layer and the corresponding double-layer structure have significant effects on the kinetics of an electrode reaction.^{56–64} In most electrochemical theories, it is supposed that the electron-transfer site is near the outer Helmholtz plane (OHP). The electron-transfer reaction is thus called an outer-sphere electron-transfer reaction. One may ignore the effect of any potential drop beyond the OHP on the reaction kinetics of an outer-sphere electron-transfer reaction unless the reaction occurs in very dilute electrolyte solution in which case some of the potential drop occurs in the diffuse double layer: the region between the OHP and the bulk solution. The effect of the potential drop in the diffuse double layer on an outer-sphere electron-transfer process

is known as the Frumkin effect.^{54,55,65} In some electrochemical reactions the electron-transfer process may occur in the inner part of the compact double layer near the inner Helmholtz plane (IHP). These processes are then called inner-sphere electron-transfer reactions. For example, the electrochemical reaction involving adsorption of reactants or those involving reactants that have a very short closest approach distance may belong to such cases. The double-layer structure will show a larger effect on the kinetics of inner-sphere electron-transfer reactions regardless of whether the electrolyte is dilute or not, since there always is a potential drop across the compact double layer. The real potential at the reaction plane, ψ_r , for an inner-sphere reaction may be significantly different from that at the OHP, ψ_o , the latter being close to the potential in bulk solution when there is excess of electrolyte present. The difference between ψ_r and ψ_o depends on a number of factors, such as the applied electrode potential, the presence of surface charge on the electrode surface, the ionic environment around the IHP, and so on.^{56–60} It is a rather complex task to evaluate the value of ψ_r and its effects on the reaction kinetics. To do so requires a full understanding of the double-layer structure, as reviewed recently by Fawcett.⁵⁶ The overall results of the potential difference between ψ_r and ψ_o might be that the observed transfer coefficient and reaction rate constant deviate significantly from their intrinsic values and may even be potential dependent.^{56–64}

It is well established that the adsorption of oxygen molecules on the electrode surface is an essential step prior to electron transfer in the reduction of oxygen on catalytic materials like Pt, although the initial adsorption state of oxygen at the solid/electrolyte interface is still controversial. The adsorbed oxygen and subsequent reaction intermediates have to replace surface-bound water molecules that form the first layer of the compact double layer. So, the electron-transfer processes involved in the electrocatalytic reduction of oxygen occur near the inner Helmholtz plane (IHP), that is, it is an inner-sphere electron-transfer reaction. Thus, it seems unreasonable to ignore the role of the structure of the double layer on the kinetics of the orr. Concerning possible double-layer effects, several factors have to be considered when analyzing the kinetics of the orr. First, the real driving potential value that the reactant and intermediates experience is different from the applied potential. This may result in a low apparent value of the transfer coefficient. Second, the adsorption of anions would not only block surface sites as is commonly stated but might also significantly change the potential near the IHP and the potential distribution in the entire double layer.

The Tafel slopes observed in the different potential regions during the orr may contain some contribution from these double-layer effects. Slopes of around -240 mV per decade in the potential region below 0.7 V suggest an apparent transfer coefficient value of 0.25 . Although this low transfer coefficient value can be explained as a change of the rate-determining step from the electron transfer to the initial adsorption of oxygen, it is also possible that the rate-determining step is still the electron-transfer step and that the low transfer coefficient value observed is due to the double-layer effect previously mentioned. Because the electron-transfer site is located within the inner Helmholtz plane, the potential difference between the electrode surface and the reaction plane would be $E - \psi_r$ which may be only a fraction, γ , of the applied potential E :

$$E - \Psi_r = \gamma E \quad (18)$$

Thus, the apparent transfer coefficient would be $\gamma\alpha$, a value smaller than the real value of α since γ is smaller than 1 . The

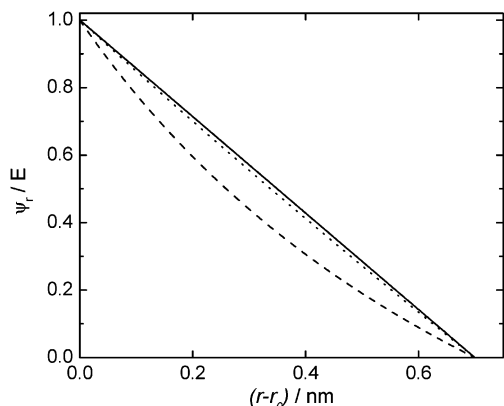


Figure 10. Potential profile inside a compact double layer formed at a catalyst particle having a radius of 500 nm (solid curve), 10 nm (short-dashed curve), and 1 nm (long-dashed curve) calculated using eq 19 (see text).

adsorption of bisulfate anions can shift the potential near the IHP negatively. This will tend to increase the value of γ . When the potential is much more positive than the PZC (potential of zero charge), the coverage of anions is so high that the potential drop occurs mainly in the inner Helmholtz layer; the γ value thus would be close to one. Under these circumstances the observed transfer coefficient becomes close to the intrinsic value of 0.5. Such effects of anion adsorption on reaction kinetics may also occur in other electrocatalytic systems involving surface adsorption of reactants or reaction intermediates. For example, the nonlinear dynamical responses obtained during the electrocatalytic oxidation of small organic molecules were found to change dramatically upon changing the anions present in solution, a result which cannot be explained by a simple surface-blocking mechanism.^{66,67} These nonlinear dynamical phenomena may become easier to understand when considering the variable potential profile across the double layer due to adsorption of different anions.

In the double layer around a particle of spherical geometry, the charges on the solution side (carried by the electrolyte ions) reside mainly on a spherical surface that is concentric with the particle and located at the distance of closest approach of the hydrated ion. The compact double layer formed thus is like a concentric spherical capacitor. If we assume that the potential drop in the diffuse double layer is negligible, then the potential profile $\psi(r)$ inside the compact layer around a particle electrode is

$$\psi(r) = \frac{r_0}{\mu} \left(\frac{r_0 + \mu - r}{r} \right) E \quad (19)$$

where r is the radial distance from the center of the particle electrode, r_0 the radius of the particle, and μ the thickness of the compact double layer. This equation has been derived by solving the Poisson equation with assumptions that the dielectric permittivity is uniform and that there is no charge inside the compact layer, that is, that no specific adsorption occurs. The thickness of the compact layer can be approximately estimated using^{54,68}

$$\mu = 2r_w + \sqrt{3}r_w + r_i \quad (20)$$

where r_w is the radius of water molecules bound to the electrode surface forming the first layer of the compact double layer and r_i is the radius of the ions that carry the charges to compensate the electrode charge. Figure 10 shows the potential profile inside

the compact double layer around particle electrodes of various radii calculated according to eq 19 using a hard sphere diameter of the water molecule of 0.29 nm⁶⁸ and assuming that the ion radius is 0.1 nm. The derivation of eq 19 assumes that the dielectric permittivity is uniform in the compact double layer and that no specific adsorption occurs. In reality, the dielectric permittivity inside the IHP is much lower than that outside of it, and the dielectric permittivity varies with distance from the electrode surface because of the variable interaction between water molecules and the electrode.^{54,57} Thus, the potential drop between the electrode surface and the IHP should be larger than that shown in Figure 10. For example, the average value of the dielectric constant of water between the IHP and the electrode surface might be only 6, whereas the average value between the IHP and OHP is about 40.⁵⁴ Correspondingly, the potential drop in the region inside of the IHP will be much larger than that predicted by eq 19. In addition, the adsorption of anions will significantly shift the potential near the IHP toward more negative values. This will further increase the potential drop inside the IHP when the electrode potential is positive of the PZC.

It can be seen that a size dependence of the potential profile in the double layer appears as the particle size shrinks to below 20 nm. At particles with radii larger than 20 nm the potential distribution is almost linear and independent of the electrode size. Such a potential distribution is identical to that in the double layer formed on a large planar electrode. When the particle radius is less than 20 nm, the potential profile gradually deviates from linear distribution and the potential drop in the inner part becomes larger. Thus, an effect of particle size on the kinetics of the electrocatalytic reduction of oxygen is expected, that is, the apparent rate constant and transfer coefficient may change with particle size. As well as the heterogeneity of dielectric permittivity and anion specific adsorption, eq 19 also ignores the effects of the flow of current on the double-layer structure. The potential profiles shown in Figure 10 depict those in an equilibrium and stationary double layer. When there is current flowing through the electrochemical cell, the double-layer structure undergoes dynamic changes.^{69–71} At small particle electrodes the current density could be very high since the current density is scaled with the reciprocal of the electrode size (e.g., see Figure 5). This may enhance the double-layer effects and cause the size effect to arise at larger particles. For example, a digital simulation by Smith et al.⁷² indicated that the double-layer effect on microelectrode voltammetry can arise when the electrode radius is below 0.1 μm even in the presence of excess supporting electrolyte.

It has been suggested that the rate-determining step of the orr might be an electron-transfer process coupled with proton transfer.^{18–20} The difference between ψ_r and ψ_o can affect the concentration of protons at the reaction plane, and this change in concentration may change the apparent rate constant and transfer coefficient of the orr. The potential drop occurring inside the IHP becomes larger at smaller particle. At potentials more positive than the PZC, this means a shift of the potential at the IHP toward more negative values, resulting in an increase in the concentration of protons and giving a larger apparent rate constant. This seems to be consistent with the larger kinetic current density observed at smaller electrodes.

In the analysis above we have provided only a rather approximate description of the double-layer effects on orr kinetics. To clarify the situation requires an accurate understanding of the dynamic structure of the double layer during anion adsorption, oxide formation, and at high current densities, an area

which still challenges modern electrochemistry. Furthermore, one has to consider the effects of the size-induced changes in the intrinsic properties of catalyst particles on the double-layer structure once the particle size is below 20 nm. A direct result of the decrease in particle size is that more metal atoms will be confined on the catalyst surface, which would cause a change of the electronic properties of metal particles. For particles in the nanoscopic or mesoscopic range, electronic properties such as the density of state (DOS) profile and electron distribution are expected to be significantly different from bulk metals. All these properties could result in dynamic changes on the structures of the double layer at the catalyst particle/electrolyte interface. We are pursuing this work with measurements using electrodes down to nanometer sizes with a defined geometry conducted at the interface between Pt and perfluorinated polymer electrolytes where the absence of specific anion adsorption may help to understand the double-layer effects on the orr kinetics.

4.3. Relevance to Fuel Cell Catalyst Layers. Our results have shown that under conditions of sufficiently high mass transport significant amounts of hydrogen peroxide may be produced during the reduction of oxygen. This has been shown to occur at platinum particles much larger than those typically used as catalyst particles within fuel cells. It is certainly true that the mass transport coefficient for an individual isolated nanometer-sized fuel cell type catalyst particle would be much larger than even the smallest of the particles we have looked at, and that as a result we would expect a smaller value of n_{eff} for that individual particle and thus a larger amount of hydrogen peroxide produced. However, as can be seen from Figure 4 and eq 11, we expect the value of n_{eff} to asymptotically approach some limiting value and become independent with mass transport coefficient. Furthermore, within a fuel cell catalyst layer we do not have individual catalyst particles separated by significant distances. Rather, all of the catalyst particles exist in close proximity. This close proximity means that the diffusion spheres around each of the particles will collide, and this will reduce the local mass transport coefficient. The degree to which this happens is rather complicated and will probably vary with position within the catalyst layer. Nonetheless, for a given catalyst layer, it should be possible to calculate an “average” mass transport coefficient for hydrogen peroxide under the operating conditions of the catalyst layer. With the use of this mass transport coefficient and Figure 4, it would then be possible to read off the expected value of n_{eff} for that particular catalyst layer and from this determine the amount of hydrogen peroxide which is expected to be formed in the catalyst layer.

The production of hydrogen peroxide would probably not significantly effect the efficiency of the fuel cell because any free peroxide will probably eventually undergo autocatalytic decomposition to water and oxygen; rather, hydrogen peroxide in the presence of transition metals may react to produce hydroxyl radicals (OH^\bullet) which in turn may lead to the degradation of the solid polymer electrolyte due to oxidative attack. Variations in the local value of $D_{\text{H}_2\text{O}_2}$ due to, for instance, changes in the amount of hydrating water in the solid polymer electrolyte, may effect changes in the local rates of production of H_2O_2 , and through this the local production rates of OH^\bullet lead to variations in membrane degradation rate.

To reduce the production of H_2O_2 , it would seem necessary to reduce the average mass transport coefficient of the fuel cell catalyst layer. Unfortunately, this approach may also have the effect of reducing the performance of the fuel cell cathode.

Alternatively, providing some mechanism to increase the adsorption strength of the peroxide on the catalyst surface or increase its subsequent decomposition may also be beneficial. Such an approach could be accomplished by alloying the Pt with other compounds, for instance, transition metals.

5. Conclusion

A new approach to study the effects of mass transport on electrochemical reactions of relevance to fuel cells has been demonstrated. We show how it is possible to investigate the oxygen reduction reaction using single-Pt-particle electrodes of submicrometer dimensions. The particle size effects on the reaction pathways and kinetics have been characterized and explored. Contrary to the size effects typically reported for experiments performed using dispersed high surface area catalysts, we see size effects occurring at much larger particle sizes. It is shown that the oxygen reduction pathway may be altered by the catalyst particle size because of variation of the mass transport rate, an area which has hitherto not received significant research. Such an effect of particle size on reaction mechanism occurs when the particle size is between 50 nm and 5 μm . These effects have not been reported before because of the inability of rotating disk measurements to access such high mass transport conditions. At potentials outside the hydrogen adsorption region on platinum when the particle is larger than 5 micrometers (mass-transfer coefficient for hydrogen peroxide or oxygen $\sim 0.04 \text{ cm s}^{-1}$, equivalent to $\sim 25\,000 \text{ rpm}$), the formation of hydrogen peroxide is negligible and virtually all oxygen molecules undergo a complete four-electron reduction to water. At particles smaller than this, progressively larger amounts of hydrogen peroxide are produced. At particles smaller than 50 nm the formation rate of hydrogen peroxide appears to become independent of the particle size since mass transport is very high and the formation rate of hydrogen peroxide is governed by the adsorption/desorption equilibrium. In this mass transport regime (mass-transfer coefficient for hydrogen peroxide or oxygen $\sim 4 \text{ cm s}^{-1}$), about 75% of oxygen molecules reacting at the surface are reduced to water and 25% are reduced to hydrogen peroxide. The comparison between the experimental results and a theoretical model suggests that a pure series or indirect mechanism is possible for oxygen reduction on Pt electrodes in sulfuric acid solution. The kinetics of the orr is rather more complex than usually believed. Anion adsorption may affect the orr not only by blocking surface sites but also by changing the potential profile within the double layer. The orr strongly depends on the potential profile in the double layer since inner-sphere electron-transfer steps are involved. The size of the catalyst particle may affect the oxygen reduction kinetics via double-layer effects as there is a dependency of the potential distribution within the double layer around a catalyst particle on that particles radius.

Acknowledgment. Financial support of this research from the Leverhulme trust is kindly acknowledged. We thank Mr. Peter Hope from LVH for kindly providing the electrophoretic paint solution. Mr. Simon Turner and Mr. Steve Atkins at the Chemistry Department of this college are thanked for their technique supports.

Appendix I. Expressions for θ_1 , θ_2 , β_1 , and β_2 .

$$\theta_1 = \frac{c_{\text{O}_2}^{\text{b}}}{\beta_1} \quad (\text{A1})$$

$$\theta_2 = \frac{\beta_2 c_{\text{O}_2}^b}{\beta_1} \quad (\text{A2})$$

$$\beta_1 = \frac{k_1 + k_2}{a_1} + \frac{a_{1-}}{a_1} + \frac{k_1 + k_2}{m_{\text{O}_2}} \quad (\text{A3})$$

$$\beta_2 = \frac{k_2}{k_3 + \frac{a_{2-}}{1 + \frac{a_2}{m_{\text{H}_2\text{O}_2}}}} \quad (\text{A4})$$

Appendix II. Kinetics Equations for the Four-Electron Reduction of Oxygen on Single Particles.

Eq 10 in the model section describes the current density for the four-electron oxygen reduction and may be rewritten as

$$\frac{1}{j} = \frac{1}{4Fk_{\text{app}}c_{\text{O}_2}^b} + \frac{1}{4Fm_{\text{O}_2}c_{\text{O}_2}^b} \quad (\text{A5})$$

where

$$k_{\text{app}} = \frac{k_1 + k_2}{\frac{k_1 + k_2}{a_1} + \frac{a_{1-}}{a_1}} \quad (\text{A6})$$

is the apparent rate constant for four-electron oxygen reduction, representing an overall rate consisting of a number of intermediate reaction steps. It is obvious that the second term on the right-hand side of eq A5, $1/(4Fm_{\text{O}_2}c_{\text{O}_2}^b)$ is the reciprocal of the steady-state limiting diffusion current density (j_L) of oxygen reduction, whereas the first term is the reciprocal of the current density for oxygen reduction when no concentration polarization occurs, that is, the kinetic current density, j_K . So, an equivalent expression to eq A5 is

$$\frac{1}{j} = \frac{1}{j_K} + \frac{1}{j_L} \quad (\text{A7})$$

This eq has the same form as the current density expression on a rotating disk electrode. In fact, eq A7 is a general current density expression for steady-state measurement methods, but the j_L term has different formulations depending on the experimental method. Although k_{app} has a complex form, we can assume it has a Butler–Volmer type of potential dependence, that is,

$$k_{\text{app}} = k_{\text{app}}^0 \exp\left[-\frac{\alpha F}{RT}(E - E^0)\right] \quad (\text{A8})$$

where E^0 is the standard equilibrium potential and k_{app}^0 and α are the apparent standard rate constant and apparent transfer coefficient of the orr, respectively. We say “apparent” because these parameters are not those for a simple electron-transfer reaction. They represent the overall results from several reaction steps including electron-transfer and adsorption steps. The assumptions required for eq A8 are that each of the individual rate constants involved in the expression of k_{app} should have a simple Butler–Volmer type dependence on the potential and that the symmetry factors (called transfer coefficients for a simple electron-transfer reaction) in the exponential term of these Butler–Volmer equations are all same. Otherwise, eq A8 does not hold. It seems unlikely that an electron-transfer process has

the same potential dependence as that of an adsorption or desorption process (i.e., the same symmetry factor), although there are other possibilities in which a simple Butler–Volmer dependence of k_{app} with potential may occur. For instance (making reference to Figure 1), when $k = k_1 + k_2 \ll a_{1-}$, the expression for k_{app} becomes

$$k_{\text{app}} = k \frac{a_1}{a_{1-}} \quad (\text{A9})$$

or when $k = k_1 + k_2 \gg a_{1-}$

$$k_{\text{app}} = a_1 \quad (\text{A10})$$

The term a_1/a_{1-} in eq A9 is actually the equilibrium constant of the adsorption/desorption of oxygen molecules. The kinetic interpretation of eq A9 is that the coverage of the adsorbed oxygen is determined mainly by the adsorption/desorption equilibrium and the electron-transfer step is the rate-determining step. The kinetic interpretation of eq A10 is that the reaction rate is governed by the rate of adsorption of oxygen.

References and Notes

- (1) Adzic, R. Recent Advances in the Kinetics of Oxygen Reduction. In *Electrocatalysis*; Lipkowsky, J., Ross, P. N., Eds.; Wiley-VCH: New York, 1998; p 197.
- (2) Markovic, N. M.; Schmidt, T. J.; Stamenkovic, V.; Ross, P. N. *Fuel Cells* **2001**, *1*, 105.
- (3) Gottesfeld, S.; Zawodzinski, T. A. Polymer Electrolyte Fuel Cells. In *Advances in Electrochemical Science and Engineering*; Alkire, R. C., Gerischer, H., Kolb, D. M., Tobias, C. W., Eds.; Wiley-VCH: Weinheim, 1997; Vol. 5, p 195.
- (4) Hsueh, K. L.; Chin, D. T.; Srinivasan, S. *J. Electroanal. Chem.* **1983**, *153*, 79.
- (5) Damjanovic, A.; Genshaw, M. A.; Bockris, J. O. M. *J. Phys. Chem.* **1964**, *45*, 4057.
- (6) Paulus, U. A.; Wokaun, A.; Scherer, G. G.; Schmidt, T. J.; Stamenkovic, V.; Markovic, N. M.; Ross, P. N. *Electrochim. Acta* **2002**, *47*, 3787.
- (7) Markovic, N. M.; Gasteiger, H. A.; Ross, P. N. *J. Phys. Chem.* **1995**, *99*, 3411.
- (8) Markovic, N. M.; Ross, P. N. In *Interfacial Electrochemistry: Theory, Experiment and Application*; Wieckowski, A., Ed.; Marcel Dekker: New York, 1999; p 131.
- (9) Markovic, N. M.; Gasteiger, H. A.; Grgur, B. N.; Ross, P. N. *J. Electroanal. Chem.* **1999**, *467*, 157.
- (10) Stamenkovic, V.; Markovic, N. M.; Ross, P. N. *J. Electroanal. Chem.* **2001**, *500*, 44.
- (11) Markovic, N. M.; Gasteiger, H. A.; Ross, P. N. *J. Electrochem. Soc.* **1997**, *144*, 1591.
- (12) Grgur, B. N.; Markovic, N. M.; Ross, P. N. *Can. J. Chem.* **1997**, *75*, 1456.
- (13) Antoine, O.; Durand, R. *J. Appl. Electrochem.* **2000**, *20*, 839.
- (14) Paulus, U. A.; Schmidt, T. J.; Gasteiger, H. A.; Behm, R. J. *J. Electroanal. Chem.* **2001**, *495*, 134.
- (15) Schmidt, T. J.; Paulus, U. A.; Gasteiger, H. A.; Behm, R. J. *J. Electroanal. Chem.* **2001**, *508*, 41.
- (16) Paulus, U. A.; Wokaun, A.; Scherer, G. G.; Schmidt, T. J.; Stamenkovic, V.; Radmilovic, V.; Markovic, N. M.; Ross, P. N. *J. Phys. Chem. B* **2002**, *106*, 4181.
- (17) Wroblowa, H. S.; Pan, Y. C.; Razumney, J. J. *Electroanal. Chem.* **1976**, *69*, 195.
- (18) Sepa, D. B.; Vojnovic, M. V.; Damjanovic, A. *Electrochim. Acta* **1981**, *26*, 781.
- (19) Sepa, D. B.; Vojnovic, M. V.; Damjanovic, A. *Electrochim. Acta* **1980**, *25*, 1491.
- (20) Damjanovic, A.; Brusica, V. *Electrochim. Acta* **1967**, *12*, 615.
- (21) Sattler, M. L.; Ross, P. N. *Ultramicroscopy* **1986**, *20*, 21.
- (22) Bregol, L. J. *Electrochim. Acta* **1978**, *23*, 489.
- (23) Watanabe, M.; Sei, H.; Stonehart, P. *J. Electroanal. Chem.* **1989**, *261*, 375.
- (24) Takasu, Y.; Ohashi, N.; Zhang, X. G.; Murakami, Y.; Mikagawa, H.; Sato, S.; Yahikozawa, K. *Electrochim. Acta* **1996**, *41*, 2595.
- (25) Peuchert, M.; Yoneda, T.; Dalla, R. A.; Boudart, M. *J. Electrochem. Soc.* **1986**, *133*, 944.
- (26) Kinoshita, K. *J. Electrochem. Soc.* **1990**, *137*, 845.

- (27) Gamez, A.; Richard, D.; Gallezot, P.; Gloaguen, F.; Faure, R.; Durand, R. *Electrochim. Acta* **1995**, *41*, 307.
- (28) Genies, L.; Faure, R.; Durand, R. *Electrochim. Acta* **1998**, *44*, 1317.
- (29) Antoine, O.; Bultel, Y.; Durand, R. *J. Electroanal. Chem.* **2001**, *499*, 85.
- (30) Gloaguen, F.; Leger, J. M.; Lamy, C.; Marmann, A.; Stimming, U.; Vogel, R. *Electrochim. Acta* **1999**, *44*, 1805.
- (31) Zoval, J. V.; Lee, J.; Gorer, S.; Penner, R. M. *J. Phys. Chem. B* **1998**, *102*, 1166.
- (32) Biswas, P. C.; Nodasaka, Y.; Enyo, M. *J. Appl. Electrochem.* **1996**, *26*, 30.
- (33) Chen, S. L.; Kucernak, A. *Electrochem. Commun.* **2002**, *4*, 80.
- (34) Chen, S. L.; Kucernak, A. *J. Phys. Chem. B* **2003**, *107*, 8392.
- (35) Chen, S. L.; Kucernak, A. *J. Phys. Chem. B* **2002**, *106*, 9396.
- (36) Chen, S.; Kucernak, A. *Angew. Chem., Int. Ed.*, submitted for publication.
- (37) Mirkin, M. V.; Bard, A. J. *Anal. Chem.* **1992**, *64*, 2293.
- (38) Oldham, K. B. In *Microelectrode: Theory and Application*; Montenegro, M. I., Queiros, M. A., Daschbach, J. L., Eds.; Kluwer: Netherlands, 1991; p 35.
- (39) Ross, P. N. In *Proceedings of the Symposium on Electrode Materials and Processes for Energy Conversion and Storage*; McIntyre, J. D. E., Srinivasan, S., Will, F. G., Eds.; The Electrochemical Society: Pennington, NJ, 1977; p 290.
- (40) Giordano, N.; Pino, L.; Arrico, A. S.; Antonucci, V.; Vivaldi, M.; Kinoshita, K. *Electrochim. Acta* **1991**, *36*, 1979.
- (41) Mirkin, M. V.; Bard, A. J. *J. Anal. Chem.* **1992**, *64*, 2293.
- (42) Gottesfeld, S.; Raistrick, I. D.; Srinivasan, S. *J. Electrochem. Soc.* **1987**, *134*, 1455.
- (43) Mello, R. M. Q.; Ticianelli, E. A. *Electrochim. Acta* **1997**, *42*, 1031.
- (44) Evans, S. A. G.; Elliott, J. M.; Andrews, L. M.; Bartlett, P. N.; Doyle, P. J.; Denuault, G. *Anal. Chem.* **2002**, *74*, 1322.
- (45) Climent, V.; Markovi, N. M.; Ross, P. N. *J. Phys. Chem. B* **2000**, *104*, 3116.
- (46) Abe, T.; Swain, G. M.; Sashikata, K.; Itaya, K. *J. Electroanal. Chem.* **1995**, *382*, 73.
- (47) Kokkinidis, G.; Jannakoudakis, D. *J. Electroanal. Chem.* **1984**, *162*, 163.
- (48) Machado, S. A. S.; Tanaka, A. A.; Gonzales, E. R. *Electrochim. Acta* **1991**, *36*, 1325.
- (49) Machado, S. A. S.; Tanaka, A. A.; Gonzales, E. R. *Electrochim. Acta* **1994**, *39*, 2591.
- (50) Uribe, F. A.; Wilson, M. S.; Springer, T. E.; Gottesfeld, S. In *Structural Effects in Electrocatalysis and Oxygen Electrochemistry*; Scherson, D., Tryk, D., Daroux, M., Xing, X., Eds.; The Electrochemical Society: Pennington, NJ, 1992; p 494.
- (51) Tarasevich, M. R.; Vilinskaya, V. S. *Elektrokhimiya* **1973**, *9*, 96.
- (52) Adzic, R. R. In *Structural Effects in Electrocatalysis and Oxygen Electrochemistry*; Scherson, D., Tryk, D., Daroux, M., Xing, X., Eds.; The Electrochemical Society: Pennington, NJ, 1992; p 419.
- (53) Oldham, K. B.; Zoski, C. G. *J. Electroanal. Chem.* **1988**, *256*, 11.
- (54) Bockris, J. O. M.; Reddy, A. K. N. In *Modern Electrochemistry*; Plenum: New York, 1970; Vol. 2.
- (55) Bard, A. J.; Faulker, L. R. *Electrochemical Methods*; John Wiley: New York, 1980.
- (56) Fawcett, W. R. Double Layer Effects in the Electrode Kinetics of Electron and Ion Transfer Reactions. In *Electrocatalysis*; Lipkowski, J., Ross, P. N., Eds.; Wiley-VCH: New York, 1998; p 322.
- (57) Fawcett, W. R. *Can. J. Chem.* **1981**, *59*, 1844.
- (58) Fawcett, W. R.; Kovacova, Z. *J. Electroanal. Chem.* **1990**, *292*, 9.
- (59) Hromadova, M.; Fawcett, W. R. *J. Phys. Chem. A* **2000**, *104*, 4356.
- (60) Hromadova, M.; Fawcett, W. R. *J. Phys. Chem. A* **2001**, *105*, 104.
- (61) Weaver, M. J.; Liu, H. Y.; Kim, Y. *Can. J. Chem.* **1981**, *59*, 1944.
- (62) Weaver, M. J. *J. Electroanal. Chem.* **2001**, *498*, 105.
- (63) Weaver, M. J.; Anson, F. C. *J. Electroanal. Chem.* **1975**, *58*, 81.
- (64) Anson, F. C.; Rodgers, R. S. *J. Electroanal. Chem.* **1973**, *47*, 287.
- (65) Frumkin, A. N. *Z. Phys. Chem.* **1933**, *146A*, 121.
- (66) Chen, S. L.; Noles, T.; Schell, M. *J. Phys. Chem. A* **2000**, *104*, 6791.
- (67) Chen, S. L.; Schell, M. *J. Electroanal. Chem.* **2001**, *504*, 78.
- (68) Fawcett, W. R. *J. Electroanal. Chem.* **2001**, *500*, 264.
- (69) Levich, B. *Dokl. Akad. Nauk SSSR* **1949**, *67*, 309.
- (70) Bonnefont, A.; Argoul, F.; Bazant, M. Z. *J. Electroanal. Chem.* **2001**, *500*, 52.
- (71) Murphy, W. D.; Manzanares, J. A.; Mafé, S.; Reiss, H. *J. Phys. Chem.* **1992**, *96*, 9983.
- (72) Smith, C. P.; White, H. S. *Anal. Chem.* **1993**, *65*, 3343.